

PAPER • OPEN ACCESS

Holographic thermal mapping in volumes using acoustic lenses

To cite this article: Ceren Cengiz and Shima Shahab 2024 *J. Phys. D: Appl. Phys.* **57** 365501

View the [article online](#) for updates and enhancements.

You may also like

- [The science case for LIGO-India](#)
M Saleem, Javed Rana, V Gayathri et al.
- [Inhibition of *Burkholderia cenocepacia* H111 quorum sensing system by environmental bacterial isolates](#)
M Wahjudi, W D Kurniawan, M T Gultom et al.
- [Quantitative modeling of bacterial quorum sensing dynamics in time and space](#)
Xiang Li, , Hong Qi et al.



EDINBURGH
INSTRUMENTS

FLS1000 MULTIMODAL PHOTOLUMINESCENCE SPECTROMETER

- + Photoluminescence Spectra, Lifetime, and Quantum Yield in One Instrument
- + Ultimate Sensitivity: Signal-To-Noise Ratio 35,000:1
- + Modular and Customisable to your Application
- + Advanced Accessories: Micro-Spectroscopy, X-Ray Excitation, Circularly Polarised Luminescence (CPL)



Discover
the FLS1000

VISIT OUR WEBSITE FOR MORE DETAILS



edinst.com

Holographic thermal mapping in volumes using acoustic lenses

Ceren Cengiz  and Shima Shahab* 

Department of Mechanical Engineering, Virginia Tech, Blacksburg, VA 24061, United States of America

E-mail: sshabab@vt.edu

Received 15 March 2024, revised 8 May 2024

Accepted for publication 5 June 2024

Published 14 June 2024



Abstract

Acoustic holographic lenses (AHLs) show great potential as a straightforward, inexpensive, and reliable method of sound manipulation. These lenses store the phase and amplitude profile of the desired wavefront when illuminated by a single acoustic source to reconstruct ultrasound pressure fields, induce localized heating, and achieve temporal and spatial thermal effects in acousto-thermal materials like polymers. The ultrasonic energy is transmitted and focused by AHL from a transducer into a particular focal volume. It is then converted to heat by internal friction in the polymer chains, causing the temperature of the polymer to rise at the focus locations while having little to no effect elsewhere. This one-of-a-kind capability is made possible by the development of AHLs to make use of the translation of attenuated pressure fields into programmable heat patterns. However, the impact of acousto-thermal dynamics on the generation of AHLs is largely unexplored. We use a machine learning-assisted single inverse problem approach for rapid and efficient AHLs' design to generate thermal patterns. The process involves the conversion of thermal information into a holographic representation through the utilization of two latent functions: pressure phase and amplitude. Experimental verification is performed for pressure and thermal measurements. The volumetric acousto-thermal analyses of experimental samples are performed to offer a knowledge of the obtained pattern dynamics, as well as the applicability of holographic thermal mapping for precise volumetric temperature control. Finally, the proposed framework aims to provide a solid foundation for volumetric analysis of acousto-thermal patterns within thick samples and for assessing thermal changes with outer surface measurements.

Supplementary material for this article is available [online](#)

Keywords: acousto-thermal patterning, sound manipulation, acoustic holographic lens, thermal holograms, acoustic holography

1. Introduction

Unwanted temperature rise typically presents problems for engineers, whereas controlled heating fills a useful role in applications such as material characterization [1], defect

detection [2–4], additive manufacturing [5–7], and thermal therapy in medical field [8, 9]. Although there are many ways to manipulate heat, ultrasound-induced thermal fields stand out in particular when it comes to the development of controlled drug-delivery systems [10, 11] and therapeutic effects [12, 13] in medical applications, as well as the remote actuation and multi-stimulus control of ultrasound-sensitive smart materials like shape memory polymers (SMPs) [14–17]. When exposed to external stimuli such as heat, these polymers can store a temporary shape and revert to their permanent or original shape. Ultrasound has been employed as a noninvasive trigger for stimulating SMP-based systems and offers the

* Author to whom any correspondence should be addressed.



Original Content from this work may be used under the terms of the [Creative Commons Attribution 4.0 licence](#). Any further distribution of this work must maintain attribution to the author(s) and the title of the work, journal citation and DOI.

ability to localize the heating action, allowing the shape recovery process to begin only in specific areas of the polymer.

Non-invasive and remote generation of ultrasound-induced heat patterns can provide numerous advantages over traditional methods of mechanical and electrical generation of temperature rise, especially if the generated thermal field can be precisely and efficiently controlled. While curved single-element and phased-array transducers are commonly used for concentrating ultrasound energy in current applications, acoustic holographic lenses (AHLs), also known as acoustic holograms, have recently emerged as a promising solution for constructing complex ultrasound fields due to their ability to manipulate ultrasound effectively [18, 19, 19–22]. AHLs, in their most basic form, record the phase profile of the required wavefront, which is then utilized to rebuild the acoustic pressure field when lit by a single acoustic source. Overall, the present popularity of acoustic holograms originates from their ease of use, durability, high resolution, and low cost, giving them an alternate option for a variety of biomedical operations [21, 23–27]. From the thermal field mapping and controlling standpoint, there has been relatively limited research on the use of AHLs to induce specific temperature fields [28, 29]. The primary challenge in creating acousto-thermal fields with AHLs arises from the non-homogeneity of the physical domain, which typically consists of a primary medium (e.g. water) and a secondary attenuating medium (e.g. polymers, tissue phantoms, sound absorbing sheets, etc). To generate the desired pressure field pattern, modeling heterogeneity necessitates computationally intensive three-dimensional full-wave simulations and iterative algorithms. Furthermore, the problem's complexity increases with the presence of mixed acousto-thermal effects and intricate heat transfer phenomena. The fundamental process of reconstructing diffraction-limited acoustic patterns requires both forward and backward propagation of the pressure field, as well as the imposition of particular boundary conditions. This is in contrast to the direct application of thermal patterns as a temperature rise in full-wave simulations, which results in unstable and non-unique solutions due to the mathematical ill-posedness of inverse heat transfer issues [30, 31]. This mismatch between the two solution strategies, one inverse and one direct, results in discrepancies between the imposed and actual pressure fields necessary for creating specific thermal patterns.

In this work, we present an effective and precise method for creating AHLs for generating specific and controllable acousto-thermal fields. For the first time, machine learning assisted inversion of the heat transfer problem is proposed for design of AHLs. The proposed approach takes into consideration the thermal effects, allowing for a comprehensive understanding and optimization of AHL thickness map for 3D production to achieve desired thermal outcomes. In addition to that, the volumetric acousto-thermal analyses of thin and thick case studies are carried out to gain a better understanding of the adaptability of AHLs for constructing tailored thermal patterns at depth. Our analyses give a thorough explanation of the

dynamics and patterns seen, as well as demonstrates the utility of ultrasound assisted holographic thermal mapping for accurate temperature control in complex volumes.

2. Methodology

The time-reversal method using three-dimensional k -space pseudospectral linear acoustical simulations is used to generate the required pressure field for constructing the desired target pattern. The selected target pattern is initially imposed as a pressure field at the target plane, using point sources distributed to match the desired pattern. As the wave propagates, the pressure field is recorded by the sensor layer situated at the top surface of the hologram plane. The collected time-varying pressure field is then reversed in time to extract frequency domain phase (ϕ_s) and amplitude (P_s) information using a windowed and zero-padded fast Fourier transform.

In the second step, the acquired pressure field is forward propagated from the hologram plane to calculate the pressure amplitude inside the volume of the target medium. The absorbed acoustic field is then converted into heat deposition to determine the temperature rise. The frequency power law, as shown in equation (1), governs sound absorption

$$\alpha = \alpha_0 f^\gamma \quad (1)$$

Here the absorption coefficient (α_0) is defined as $4.2 \text{ dB MHz cm}^{-1}$ for Smooth-On Ecoflex 00–10 [32], a commercially available soft silicone rubber widely employed as a tissue-mimicking material in the literature [33–35]. The absorption coefficient is defined as $0.0022 \text{ dB MHz cm}^{-1}$ for the surrounding water medium, and the power law absorption exponent (γ) of 1.1 is chosen for the whole domain. Excitation frequency (f) of 1 MHz is selected for the source according to the typical frequency range for therapeutic ultrasound applications [36]. Additionally, for water and silicone rubber, the density and speed of sound are adjusted as follows $\rho_w = 1000 \text{ kg m}^{-3}$, $c_w = 1481 \text{ m s}^{-1}$, $\rho_t = 1040 \text{ kg m}^{-3}$ [32] and $c_t = 1020 \text{ m s}^{-1}$ [37], respectively. The computational domain consists of 350×350 pixels, with a grid size of 0.2 mm. Additionally, the domain is expanded with perfectly matched layers to prevent undesired reflections from model boundaries. The desired pressure field within the sample medium is enforced as Dirichlet boundary conditions in the simulations.

The acousto-thermal analysis of the sample material is conducted layer by layer at depth throughout the paper, utilizing the following notations for easy understanding and concise representation. The initial layer (h_0) depicts the separation between the sample and the hologram plate's top surface. The uppermost surface of the sample is indicated by (h_n), and the target layer on which a particular pattern is imposed is designated by (h_t). The overall sample material thickness is determined by the difference between the top and bottom layers ($h_n - h_0$), figure 1(d).

The volumetric heat deposition (q) in the sample material, resulting from the conversion of acoustic energy into thermal

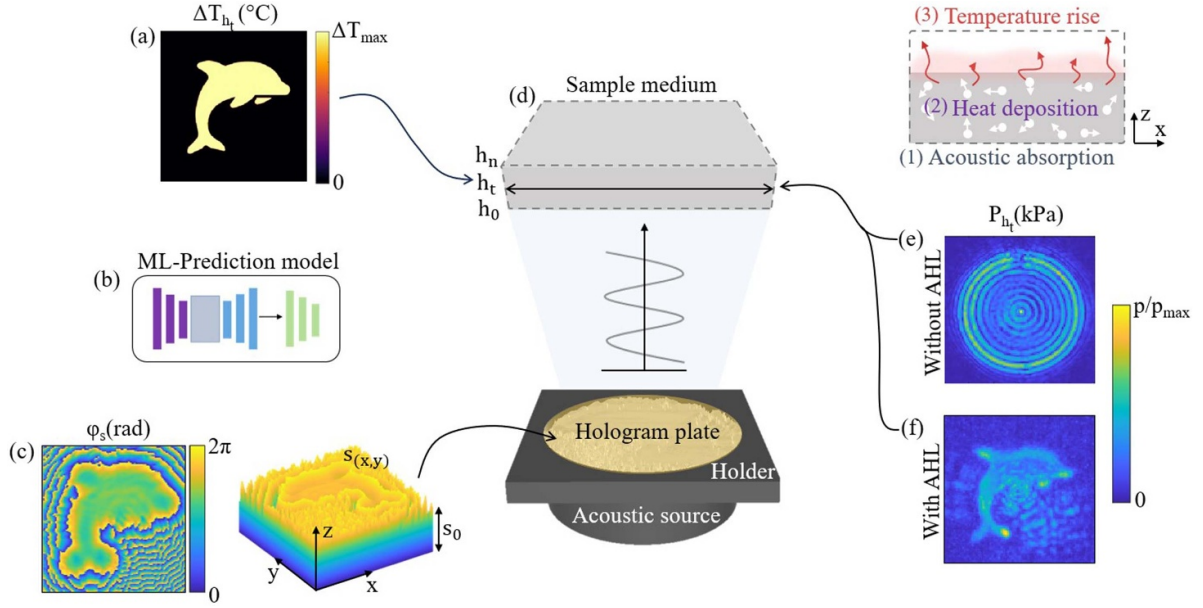


Figure 1. The holographic acousto-thermal patterning workflow. (a) Selected thermal pattern for the target layer at depth (h_t). (b) Illustration of the deep learning-based model for acoustic source prediction. (c) The output of the source phase pattern (left) and generated thickness map (right). (d) A holographic ultrasound system for acoustic to thermal transformation is depicted schematically. Measured acoustic pressure amplitude at the target layer (e) without the acoustic holographic lens (AHL) and (f) with AHL (experimental pressure field measurements are conducted in deionized water only).

energy due to pressure field (p) attenuation owing to absorption, is calculated using the relation [38]:

$$q = \alpha p^2 / \rho_t c_t \quad (2)$$

Following that, the resulting temperature rise is then calculated using Penne's Bio Heat equation [39]:

$$\rho_t C_t \frac{\partial T}{\partial t} = \nabla \cdot (\kappa \nabla T) + q_b + q \quad (3)$$

Because this study uses a soft silicone rubber with no fluid flow inside, convection due to blood flow (q_b) is neglected, and only heat deposition and diffusion effects are taken into account for estimating temperature fluctuations. Thermophysical properties of the sample material are set to $\kappa = 0.16 \text{ W mK}^{-1}$ [40] and $C_t = 1558 \text{ J kgK}^{-1}$ [41] in equation (3) for calculating thermal conductivity and specific heat capacity, respectively. The initial temperature of the entire domain is set to $25 \text{ }^\circ\text{C}$, in accordance with the experimental boundary conditions. During simulations, the surrounding water medium remains constant while the tissue medium is subjected to acoustic heating, with the ultrasound exposure duration set to 10 s.

To generate precisely targeted acousto-thermal patterns, discrepancies between the imposed and forward-propagated pressure fields necessitate iterative simulations and processing efforts. In a variety of applications, deep learning techniques have been offered as a solution to inverse heat and design problems [42–48]. For the first time, we use a machine learning (ML) system to compress the process into a single inverse issue for speedy and efficient holographic plate design. The

deep learning network utilized in this study adopts a convolutional neural network structure based on the U-Net architecture, which consists of encoder and decoder blocks. We employ a generative adversarial network framework following the structure introduced by Isola *et al* [49]. This framework is adapted to convert thermal information into a holographic representation by utilizing two latent functions: pressure phase and amplitude. The model receives images of thermal patterns and processes them through successive convolutional layers to extract features. Subsequently, the network outputs the pressure field (both amplitude and phase) based on the input thermal field. The training set for the network was generated using an in-house MATLAB code, implementing the acousto-thermal time-reversal modeling approach. The dataset comprises 542 pairs of thermal and pressure fields, which were split into training, validation, and test sets with proportions approximately 70%, 15% and 15%, respectively. For adversarial training, the discriminator model uses binary cross-entropy (BCE) loss calculations to quantify differences between the ground truth and synthesized pressure maps:

$$BCE = -(\hat{GT}) \log(GT_{pr}) + (1 - \hat{GT}) \log(1 - \hat{GT}). \quad (4)$$

Here \hat{GT} represents the ground truth and GT_{pr} the prediction probability. Aside from BCE, the mean absolute error (MAE) is used for pixel-wise error assessment to evaluate the generator model's performance for predicting (Est) the desired pressure field information. Once the created ML algorithm captures the internal characteristics of the case, desired pressure field information can be retrieved by feeding the model the selected thermal pattern.

$$\text{MAE} = \frac{1}{n_{\text{step}}} \sum_{m=1}^{n_{\text{step}}} \left| G\hat{T}_m - \text{Est}_m \right|. \quad (5)$$

Essentially, the proposed ML platform allows for predicting AHLs with the thermal pattern as the primary focus. This approach offers versatility in cases where heat transfer dynamics cannot be separated from the problem. While traditional pressure field-based techniques lack the capability to adequately modulate the pressure field for generating the desired thermal patterns, our proposed acousto-thermal approach allows heat transfer related parameters to alter the thickness map for application-based usage of AHLs. Moreover, ML driven technique simplifies the AHL design process by remaining unaffected by the complexity of mixed acousto-thermal effects related to heat transfer dynamics.

The next step is to transform the ML model's output ϕ_s and P_s into a Phase-Only-Hologram (POH) to build the final thickness map for 3D printing. This is accomplished through the use of bidirectional error diffusion [50] for phase modification. In contrast to the original approach, which used a constant amplitude of 1 for the raw pixels, we used a pattern-adaptive optimization parameter to improve the quality of the empirically reconstructed image [51]. Finally, the thickness map for 3D printing is calculated using the following formula [18]:

$$s_{(x,y)} = s_0 - \frac{\Delta\phi_{(x,y)}}{k_w - k_h}. \quad (6)$$

Here, each pixel's thickness in the hologram plane is indicated by $s_{(x,y)}$, the phase-lag between source and POH is represented by $\Delta\phi_{(x,y)}$, and the hologram plate's initial thickness is specified as s_0 . The wave numbers for hologram material and surrounding medium are defined as k_h and k_w , respectively. Considering that the sound propagation through the AHL involves multiple mediums, variations in transmitted acoustic power compared to the input power is expected. To quantify and control the impact of impedance mismatch, transmission coefficient (TR) given by Melde *et al* [18], is also considered. AHLs are fabricated through stereolithography (SLA) techniques using the Form 2 resin printer by Formlabs; capable of achieving a printing resolution ranging from $25\ \mu\text{m} - 100\ \mu\text{m}$. Acoustic properties of the photo-polymer (Clear Resin) are $\rho_h = 1178\ \text{kg m}^{-3}$, $c_h = 2594\ \text{m s}^{-1}$ and $\alpha_0 = 2.92\ \text{dB MHz}^{-y}\ \text{cm}^{-1}$ [52] and the final thickness of the lens is 6 mm, figure 2(a). Ecoflex 00–10 testing samples are made by combining two liquid ingredients in a 1:1 ratio. The liquid mixture is injected into a controlled-height silicone mold to achieve the appropriate sample thickness ($h_n - h_0$) and cured at room temperature. For the experimental testing, two case studies are studied: $h_n - h_0 = 1\ \text{mm}$ (thin) and $h_n - h_0 = 30\ \text{mm}$ (thick) samples.

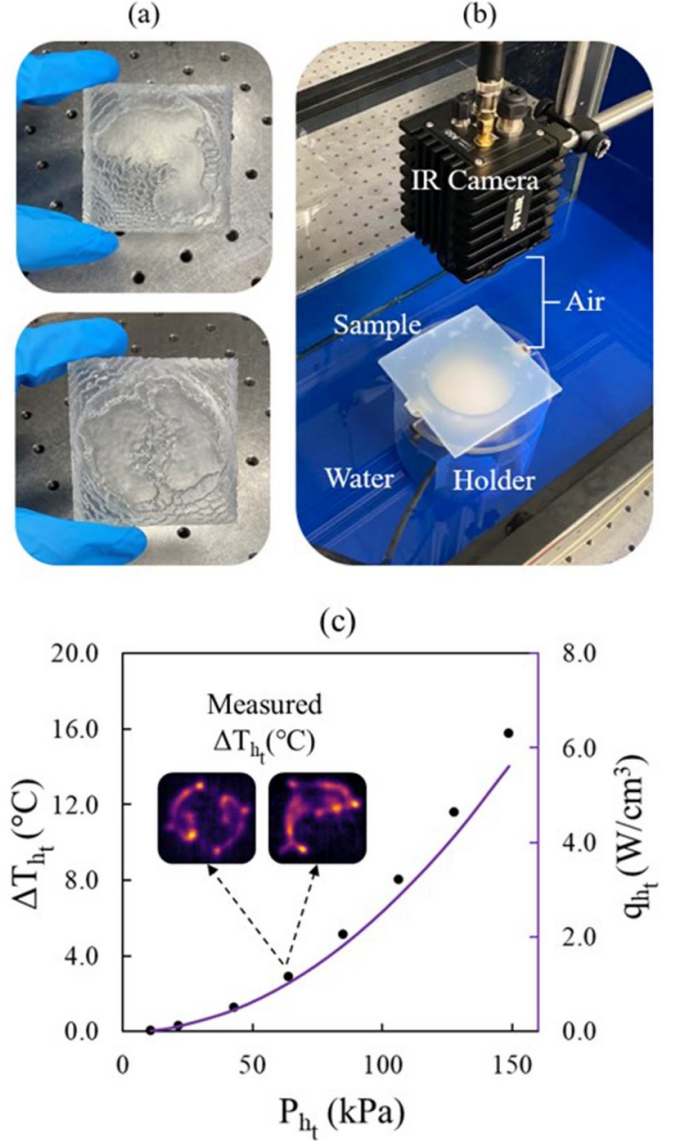


Figure 2. (a) 3D printed hologram plates for testing. (b) Experimental setup for the thermal measurements. (c) Relationship between heat deposition, temperature rise, and acoustic pressure amplitude at the target layer in a thin sample with a 1 mm thickness. Additionally, a reference measurement point for the experiment is shown.

3. Results and discussion

3.1. Pressure field measurements

The study's experimental verification is divided into two steps: pressure and thermal measurements. Both experiments are carried out in a tank of degassed and deionized water. Precision Acoustics, Ltd's Aptflex F28 acoustic absorbing sheets are used to ensure acoustic isolation in a section of the tank. The transducer and acoustic hologram are held in place by an in-house holder. Acoustic source used in the experiments is a flat transducer made of a 50 mm diameter piezoelectric disk

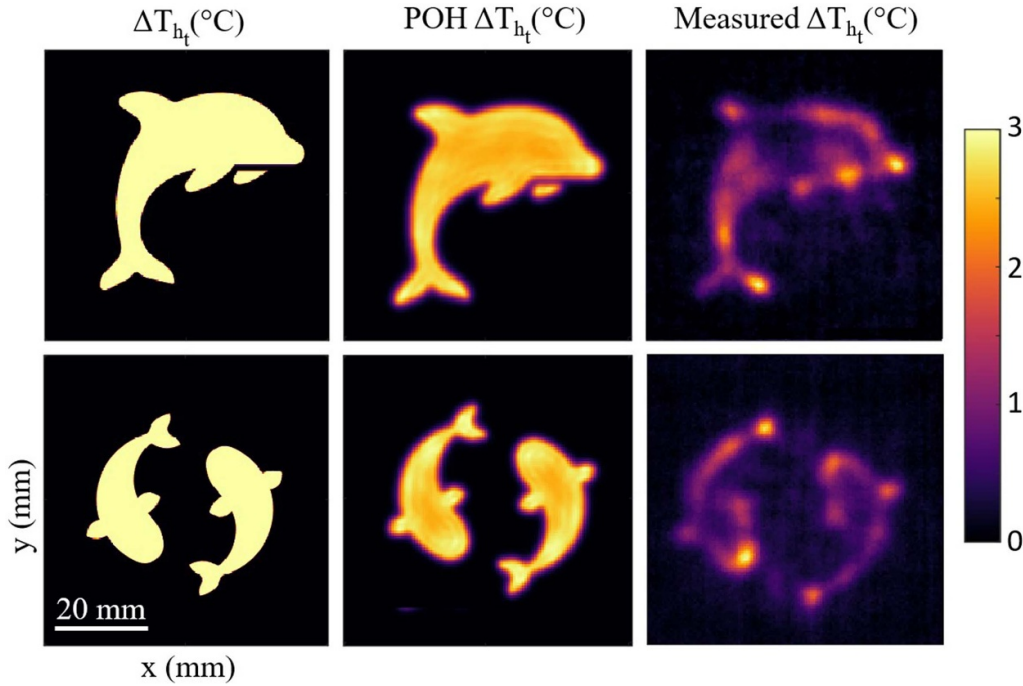


Figure 3. Thermal maps for two different patterns with a continuous ultrasonic exposure period of 10 s. ΔT_{h_t} , POH ΔT_{h_t} and Measured ΔT_{h_t} represent input thermal maps to the ML model, simulation and experimental results respectively.

that operates at 1 MHz and it is excited with a sinusoidal burst signal consisting of 20 cycles at 10 ms intervals for pressure field measurements. A signal generator (Keysight 33 500B) and an amplifier (E&I A075) is used to power the transducer. Pressure amplitude mapping is performed using a needle hydrophone (ONDA HNR-0500) connected to a 3D positioning system. A calibration factor of -252.81 dB (re. $1 \text{ V } \mu\text{P}^{-1}$ at 1 MHz), provided by the manufacturer, is used to convert the voltage data into acoustic pressure information. An oscilloscope (Tektronix TBS2104) is used to visualize the sampled digital signal, and the recorded signals are post-processed using a MATLAB software. To cover the complete pattern at the target plane, a 60×60 mm scanning zone with a 0.5 mm step size is chosen ($h_t = 23$ mm). 3D-printed AHLs for two different target shapes are depicted in figure 2(a) for reference. The resulting pressure field measurements are given in figures 1(e) and (f). A clear dolphin pattern conversion is clearly visible when the transducer pressure field, figure 1(e), is compared with the hologram incorporated pressure amplitude distribution, figure 1(f), at the target plane. While a satisfactory normalized pressure field pattern is obtained, undesirable pressure amplitudes are found in the outer areas. This is mainly because the hologram plate was designed to create a thermal pattern on a sample material, while hydrophone scans were conducted exclusively in the water domain. Overall, hydrophone measurements provide useful insights about the holographic plate's performance prior to thermal measurements, allowing us to adjust the transducer's operational settings for the upcoming acousto-thermal conversion,


figure 2(c). For more details on the pressure field variation and efficiency calculations in the presence of AHL, readers can refer to supplementary material note S1.

3.2. Thermal field measurements: thin sample

Next, an upgraded mobile part is added to the holder design for the second phase of the experimental arrangement, figure 2(b), to secure the sample material at a certain distance h_0 from the hologram surface. Infrared (IR) thermal camera (FLIR A50-51°, Teledyne FLIR LLC) with IR resolution of 464×348 and thermal sensitivity of <35 mK [35] is employed to measure the thermal distribution. Following transducer activation, the recording length is set to 10 s, with 30 frames taken each second. Thermal pictures are also preserved for later post-processing, beginning with thermal equilibrium. Furthermore, the region between the IR camera and the upper surface of the sample is retained as air to prevent any undesired IR emission by water. The measurements are taken at room temperature and humidity. The emissivity of the silicone rubber is set as $\epsilon = 0.9$ for the measurement.

Thermal measurement results are compared in figure 3 for two different selected patterns (dolphin and yin-yang fish). The first experimental analysis is done for the $h_n - h_0 = 1$ mm thin sample where $h_n = h_t = 23$ mm. The results show that a maximum temperature difference of 3°C can be achieved across all cases for the 10-s heating time. Error metrics given in equations (7)–(10) are used for performance evaluation of the reconstructed thermal images.

Table 1. Error calculation results for the simulated and measured thermal maps with respect to the imposed thermal field. High PSNR, low RMSE and a high SSIM is indicative of high quality.

	ΔT_{h_t}	PSNR (dB) \uparrow	RMSE \downarrow	SSIM \uparrow
	POH ($^{\circ}\text{C}$)	13.95	0.20	0.76
	Measured ($^{\circ}\text{C}$)	12.73	0.23	0.33
	POH ($^{\circ}\text{C}$)	13.95	0.20	0.76
	Measured ($^{\circ}\text{C}$)	10.73	0.29	0.32

$$\text{PSNR} = 10 \log_{10} \frac{\text{MAX}^2}{\text{MSE}} \quad (7)$$

$$\text{MSE} = \frac{1}{ab} \sum_{i=1}^a \sum_{j=1}^b [(\hat{\Delta T}(i,j) - \Delta T(i,j))^2] \quad (8)$$

$$\text{RMSE} = \sqrt{\text{MSE}} \quad (9)$$

$$\text{SSIM} = \frac{(2\mu_x\mu_y + L_1)(2\sigma_{xy} + L_2)}{(\mu_x^2 + \mu_y^2 + L_1)(\sigma_x^2 + \sigma_y^2 + L_2)} \quad (10)$$

Here MAX is the maximum pixel value, which can be evaluated using $2^D - 1$, where D is the dynamic range of either the measured ΔT or POH ΔT . In equation (8), $\hat{\Delta T}$ represents the ground truth thermal map, while ΔT is the numerical or the experimental thermal map results. Rows and columns of the data matrix are denoted by i, a and j, b respectively. In the calculation of SSIM (equation (10)), μ_x and μ_y denote the local mean values, σ_x^2 and σ_y^2 represent the variances, and L_1 and L_2 are the stability constants.

A comparison of error metrics is presented in table 1. Overall, the root mean squared error (RMSE) values for both the simulation and experimental thermal maps are calculated to be less than 0.3, indicating a tight match between the imposed and acquired temperature elevation. The average peak signal-to-noise (PSNR) value across all four examples is 12.84 dB, with the simulated POH ΔT giving higher precision for thermal patterning (13.95 dB), as expected. PSNR of experimentally measured ΔT thermal images of dolphin and yinyang patterns are calculated as 12.73 dB and 10.73 dB, respectively. Additionally, structural similarity index (SSIM) calculations are revealed a SSIM value of 0.76 for the simulated POH ΔT , which is an indicator for high quality reconstruction. Notably, in experimental settings, this value decreases to 0.3, largely attributed to the low resolution of the images captured by the IR camera. All in all, given the experimental errors, such as 3D printing tolerances for the hologram plate, material imperfections, and unwanted IR reflections during thermal camera measurements, machine learning-generated holograms offered a promising solution to fast and accurate acousto-thermal patterning.

3.3. Thermal field measurements: thick sample

In addition to the single-layer study, acousto-thermal patterning capability is also tested for a thicker sample $h_n - h_0 = 30\text{mm}$, as given in figure 4. Following a similar technique as used with the thin sample, a new hologram plate is carefully designed to target a specific layer within the

thicker sample, with point sources distributed within the layers to accurately impose the desired pattern. Thick sample temperature evaluations include two basic steps: (1) experimental measurements as described in section 3.2 (figure 2). An infrared (IR) thermal camera is used to measure the temperature distribution of the thick sample upper surface, and the results are shown in figure 4(b). The measured surface patterns in figure 4(b) are validated by comparing maximum temperature and pattern boundaries to the pattern generated from the acousto-thermal computational modeling described in section 2, equations (1)–(3). It is crucial to highlight that our computational modeling was previously validated for the thin sample (in section 3.2) by comparing the computational modeling findings to the measurements in figure 3 and table 1. (2) Applying acousto-thermal modeling to layer-by-layer computations. Solving equation (3), a volumetric bio-heat equation in which temperature $T = T(x,y,z)$, we may obtain the temperature distribution throughout the entire volume of the supplied sample. The weighted average temperature variation is then obtained for each layer, using equations (11) and (12), and translated into a binary map, equations (13) and (14), for predicting the temperature pattern distribution in any target layer of the thick sample. Figures 4(e.1) and (e.2) provides an examination of the thermal pattern variation at depth, while the graph in figure 4(f.1) illustrates the normalized maximum temperature variation as the distance from the target layer changes. The following calculations are made to evaluate the pattern distribution:

$$|\Delta T_{\text{layer}}(i,j)| = \frac{\Delta T_{\text{layer}}(i,j)}{\Delta T_{h_t, \text{max}}} \quad (11)$$

$$\overline{\Delta T_{\text{layer}}} = \frac{1}{ab} \sum_{i=1}^a \sum_{j=1}^b |\Delta T_{\text{layer}}(i,j)| \quad (12)$$

$$B_{\text{layer}}(i,j) = \begin{cases} 1 & \text{if } |\Delta T_{\text{layer}}(i,j)| \geq \overline{\Delta T_{\text{layer}}} \\ 0 & \text{otherwise} \end{cases} \quad (13)$$

$$B_{\text{layer}}(i,j) = B_{\text{layer}}(i,j) \cdot \overline{\Delta T_{\text{layer}}} \quad (14)$$

Here, the subscript ‘layer’ refers to the specific layer being analyzed, which lies between h_0 and h_n . In equation (11), $|\Delta T_{\text{layer}}(i,j)|$ indicates the normalized temperature variation for the layer, adjusted relative to the maximum temperature of the h_t which represents the desired temperature rise within the thick sample medium. Furthermore, $\overline{\Delta T_{\text{layer}}}$ represents the average normalized temperature variation, reflecting the average conditions within each layer. Equations (13)

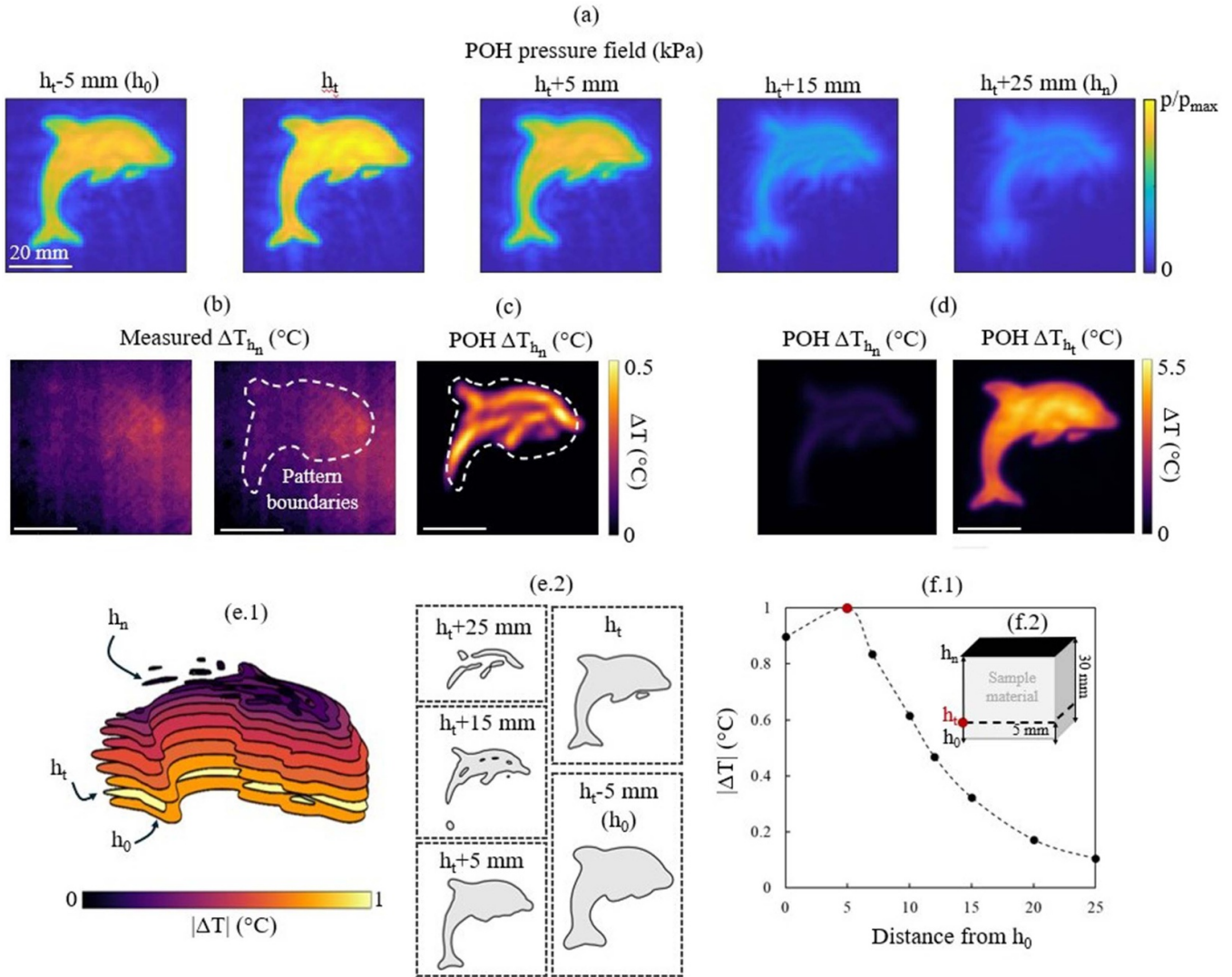


Figure 4. Volumetric analysis for the 30 mm thick sample. (a) Pressure field variation between layers. (b) IR camera measurement for the top surface (h_n). For visual comparison, pattern boundaries are indicated. The simulation thermal map for layers (c) h_n with experimental colormap boundaries and (d) h_n and h_t with simulation colormap boundaries. (e.1) Volumetric representation of the layer-by-layer pattern variation and normalized temperature rise $\Delta T/\Delta T_{\max,h_t}$. (e.2) Weighted average temperature rise is converted into a binary map for pattern comparison. (f.1) Temperature variation in normalized simulation data by distance from the bottom layer. (f.2) The layer distances inside the sample material are depicted schematically.

and (14) outline the procedures for transforming these temperature data into binary maps. Specifically, values in the binary maps are set to 1 if they exceed the layer’s normalized average temperature, and to 0 otherwise, as shown in figure 4(e.2). This method of binarization helps illustrate the pattern behavior as a weighted average temperature rise, enhancing our understanding of the thermal patterns and facilitating the tuning of the acousto-thermal hologram for precise pattern control. The results of these calculations and their implications for the contour map representations are further explored in the volumetric representations displayed in figure 4(e.1), where the normalized average temperatures multiplied by the binary map to assign these values to the pattern distribution.

A well-defined dolphin pattern at the chosen target layer is obtained, with a noticeable increase in heat buildup towards

the pattern’s center as one goes away from the target surface, coupled by a drop in the maximum temperature rise. This behavior is also observed in the layer-by-layer pressure field variation depicted in figure 4(a). From layer h_t and above, the pressure field is more focused at regions inside the dolphin pattern, while the outline of the pattern becomes fainter. However, in contrast to the thermal pattern, the dolphin shape remains relatively distinct even in the pressure field at the top layer. This phenomenon can be attributed to the reduction in heat deposition resulting from ultrasonic absorption beyond h_t+15 mm, leading to a predominance of heat diffusion through thermal conduction within the material volume. Patterns depicted in figure 4(e.2) clearly demonstrate this phenomenon, with weighted average temperature rise only evident at the center spots as the distance from the target layer increases, while the rest of the dolphin pattern

is not visible due to thermal uniformity. Experimentally, the same behavior is seen, as illustrated in the comparison between figures 4(b)–(d). While direct experimental verification of layer-by-layer thermal patterns is not feasible due to surface-constrained measurements using an IR camera, readers interested in obtaining additional surface measurements across various thicknesses are encouraged to refer to Note S2 in supplementary material. Notably, the authors' future communication will focus on alternate measuring approaches, such as using thermochromic color-changing materials [53] and MR Thermography [54], to capture temperature distributions in greater detail. However, these approaches necessitate considerable changes to our current experimental setup and are currently challenging. Yet, we acknowledge the importance of detailed experimental validations for layer-by-layer thermal analysis. Nonetheless, when studying the pattern boundaries, the top layer thermal map comparison shows a close match between simulation and experiment data. For 10 s of ultrasound exposure time, a temperature rise up to 0.5°C is observed at the h_n . As indicated in the graph in figure 4(c), this nearly corresponds to a 5.5°C temperature rise at the h_t where a well-defined dolphin pattern is visible.

4. Conclusion

A novel machine learning-assisted holographic approach for acousto-thermal patterning in soft material samples was proposed in this study. We presented thorough analyses that include both numerical calculations and experimental validations to demonstrate how 3D-printed AHLs may be utilized to modulate sound to create heat maps. We compared two different arbitrary target shapes based on the well-known image quality parameters. During the final step of our research, we focused on volumetric analysis and layer-by-layer pattern variation inside a thick soft sample. We were able to establish a clear thermal pattern at the target layer, and as we moved away from the target zone, the thermal effect and pattern clarity gradually faded. Pattern focusing was achieved by combining a simple flat transducer with an acoustic hologram without the need for a curved or phased array transducer. The proposed acousto-thermal modeling approach enables applying precise volumetric temperature control of sample materials which is crucial for studying thermal phenomena and optimizing for broad application. Moreover, with the AHL's easy adaptability introduced through the acousto-thermal based approach, holographic lens design can be expanded to address multiple focal points and volumes simultaneously. Notably, the framework, which can correlate with surface temperature data alone, offers a solid platform for forecasting and evaluating thermal changes within materials using only outer surface measurement. Further investigation into this feature of our methodology has the potential to generate practical benefits and could be a future research topic of interest. Overall, because of their specific features and capabilities, AHLs

hold considerable promise for developing volumetric thermal holography for future applications in therapeutic ultrasound, material characterization, additive manufacturing, and non-invasive actuation of ultrasound-sensitive smart materials. Finally, our paper introduces a paradigm shift in thermal AHL research by integrating heat transfer effects into the design process for generating acousto-thermal fields. This innovative approach enables the incorporation of complex features of sample mediums, including non-uniform thermophysical properties, various heat transfer mechanisms, changing heating durations, and other factors, into the evaluation of the thickness map of the AHL. As a result, it facilitates the efficient and effective design of 3D printed holographic lenses tailored to specific applications. In accordance with this, our aim is to provide a flexible and customized framework that bridges the gap between physics and engineering, with an emphasis on machine learning-assisted developments in AHL studies. Looking forward, we envision the creation of a comprehensive acousto-thermal database through big data-driven analytics. This initiative will enable the algorithm to be trained on a diverse array of acousto-thermal scenarios, empowering it to deliver tailored solutions for specific cases. By incorporating additional parameters and refining the feedback mechanism, we aim to further enhance the algorithm's capability to address the challenges encountered in real-life applications. This approach holds significant promise for advancing acousto-thermal engineering and addressing complex problems in various fields. Furthermore, exploring in-depth measurements using alternative techniques like thermochromic color-changing materials and MR thermography could enrich our understanding, providing a more comprehensive review of the pattern formation for the refinement of our proposed methodology.

See supplementary material note S1. for experimental analysis of pressure field variation in the presence of AHL, and Note S2. for the additional IR camera measurements.

Data availability statement

All data that support the findings of this study are included within the article (and any supplementary files).

Acknowledgments

This work was supported by the U.S. National Science Foundation (NSF) under the Grants, Award No. CAREER CMMI 2143788, and CMMI 2016474, which are gratefully acknowledged.

ORCID iDs

Ceren Cengiz  <https://orcid.org/0000-0003-4420-4171>
Shima Shahab  <https://orcid.org/0000-0003-1970-5345>

References

- [1] Jones A 2014 *Temperature-Programmed Reduction for Solid Materials Characterization* (CRC Press)
- [2] Ibarra-Castanedo C, Piau J-M, Guilbert S, Avdelidis N P, Genest M, Bendada A and Maldague X P 2009 Comparative study of active thermography techniques for the nondestructive evaluation of honeycomb structures *Res. Nondestruct. Eval.* **20** 1
- [3] Ibarra-Castanedo C, Tarpani J R and Maldague X P 2013 Nondestructive testing with thermography *Eur. J. Phys.* **34** S91
- [4] Favro L, Han X, Ouyang Z, Sun G, Sui H and Thomas R 2000 Infrared imaging of defects heated by a sonic pulse *Rev. Sci. Instrum.* **71** 2418
- [5] Buchanan C and Gardner L 2019 Metal 3D printing in construction: a review of methods, research, applications, opportunities and challenges *Eng. Struct.* **180** 332
- [6] Herzog D, Seyda V, Wycisk E and Emmelmann C 2016 Additive manufacturing of metals *Acta Mater.* **117** 371
- [7] Rosli N A, Alkahari M R, Abdollah M F bin, Maidin S, Ramli F R and Herawan S G 2021 Review on effect of heat input for wire arc additive manufacturing process *J. Mater. Res. Technol.* **11** 2127
- [8] Moros E 2012 *Physics of Thermal Therapy: Fundamentals and Clinical Applications* (CRC Press)
- [9] Arora D, Minor M A, Skliar M and Roemer R B 2006 Control of thermal therapies with moving power deposition field *Phys. Med. Biol.* **51** 1201
- [10] Han J, Fei G, Li G and Xia H 2013 High intensity focused ultrasound triggered shape memory and drug release from biodegradable polyurethane *Macromol. Chem. Phys.* **214** 1195
- [11] Needham D and Dewhurst M W 2001 The development and testing of a new temperature-sensitive drug delivery system for the treatment of solid tumors *Adv. Drug Deliv. Rev.* **53** 285
- [12] Jenne J W, Preusser T and Günther M 2012 High-intensity focused ultrasound: principles, therapy guidance, simulations and applications *Z. Med. Phys.* **22** 311
- [13] Escoffre J-M and Bouakaz A 2015 *Therapeutic Ultrasound* vol 880 (Springer)
- [14] Peng K, Shahab S and Mirzaeifar R 2020 Interaction of high-intensity focused ultrasound with polymers at the atomistic scale *Nanotechnology* **32** 045707
- [15] Bhargava A, Peng K, Stieg J, Mirzaeifar R and Shahab S 2017 Focused ultrasound actuation of shape memory polymers; acoustic-thermoelastic modeling and testing *RSC Adv.* **7** 45452
- [16] Delaey J, Dubruel P and Van Vlierberghe S 2020 Shape-memory polymers for biomedical applications *Adv. Funct. Mater.* **30** 1909047
- [17] Li G, Fei G, Liu B, Xia H and Zhao Y 2014 Shape recovery characteristics for shape memory polymers subjected to high intensity focused ultrasound *RSC Adv.* **4** 32701
- [18] Melde K, Mark A G, Qiu T and Fischer P 2016 Holograms for acoustics *Nature* **537** 518
- [19] Brown M D, Cox B T and Treeby B E 2020 Stackable acoustic holograms *Appl. Phys. Lett.* **116** 261901
- [20] Bakhtiari-Nejad M, Elnahas A, Hajj M R and Shahab S 2018 Acoustic holograms in contactless ultrasonic power transfer systems: Modeling and experiment *J. Appl. Phys.* **124** 244901
- [21] Sallam A, Meesala V C, Hajj M R and Shahab S 2021 Holographic mirrors for spatial ultrasound modulation in contactless acoustic energy transfer systems *Appl. Phys. Lett.* **119** 144101
- [22] Zhang J, Tian Y, Cheng Y and Liu X 2020 Acoustic holography using composite metasurfaces *Appl. Phys. Lett.* **116** 030501
- [23] Jiménez-Gambín S, Jiménez N, Pouliopoulos A N, Benlloch J M, Konofagou E E and Camarena F 2022 Acoustic holograms for bilateral blood-brain barrier opening in a mouse model *IEEE Trans. Biomed. Eng.* **69** 1359
- [24] Jiménez-Gambín S, Jiménez N, Benlloch J M and Camarena F 2019 Holograms to focus arbitrary ultrasonic fields through the skull *Phys. Rev. Appl.* **12** 014016
- [25] Kim J, Kasoji S, Durham P G and Dayton P A 2021 Acoustic holograms for directing arbitrary cavitation patterns *Appl. Phys. Lett.* **118** 051902
- [26] Randad A, Ghanem M A, Bailey M R and Maxwell A D 2020 Design, fabrication and characterization of broad beam transducers for fragmenting large renal calculi with burst wave lithotripsy *J. Acoust. Soc. Am.* **148** 44
- [27] Sallam A and Shahab S 2022 On nonlinear effects in holographic-modulated ultrasound *Appl. Phys. Lett.* **121** 204101
- [28] Andrés D, Vappou J, Jiménez N and Camarena F 2022 Thermal holographic patterns for ultrasound hyperthermia *Appl. Phys. Lett.* **120** 084102
- [29] Andrés D, Rivens I, Mouratidis P, Jiménez N, Camarena F and Haar G T 2023 Holographic focused ultrasound hyperthermia system for uniform simultaneous thermal exposure of multiple tumor spheroids *Cancers* **15** 2540
- [30] Ozisik M N 2018 *Inverse Heat Transfer: Fundamentals and Applications* (Routledge)
- [31] Alifanov O M 2012 *Inverse Heat Transfer Problems* (Springer)
- [32] Smooth-On E Ecoflex™ 00-10 (available at: www.smooth-on.com/products/ecoflex-00-10)
- [33] Adams F, Qiu T, Mark A, Fritz B, Kramer L, Schlager D, Wetterauer U, Miernik A and Fischer P 2017 Soft 3D-printed phantom of the human kidney with collecting system *Ann. Biomed. Eng.* **45** 963
- [34] Bowen D L, Touchet T J, Maitland D J and McDougall M P 2023 Technical note: the design and validation of a multi-modality lung phantom *Med. Phys.* **50** 4809
- [35] Estermann S-J, Pahr D H and Reisinger A 2020 Quantifying tactile properties of liver tissue, silicone elastomers and a 3D printed polymer for manufacturing realistic organ models *J. Mech. Behav. Biomed. Mater.* **104** 103630
- [36] Speed C 2001 Therapeutic ultrasound in soft tissue lesions *Rheumatology* **40** 1331
- [37] Mark J E *et al* 2007 *Physical Properties of Polymers Handbook* vol 1076 (Springer)
- [38] Bailey M, Khokhlova V, Sapozhnikov O, Kargl S and Crum L 2003 Physical mechanisms of the therapeutic effect of ultrasound (a review) *Acoust. Phys.* **49** 369
- [39] Pennes H H 1948 Analysis of tissue and arterial blood temperatures in the resting human forearm *J. Appl. Physiol.* **1** 93
- [40] Bhanushali S, Ghosh P C, Simon G P and Cheng W 2017 Copper nanowire-filled soft elastomer composites for applications as thermal interface materials *Adv. Mater. Interfaces* **4** 1700387
- [41] Cabibihan J-J, Joshi D, Srinivasa Y M, Chan M A and Muruganatham A 2015 Illusory sense of human touch from a warm and soft artificial hand *IEEE Trans. Neural Syst. Rehabil. Eng.* **23** 517
- [42] Jambunathan K, Hartle S, Ashforth-Frost S and Fontana V 1996 Evaluating convective heat transfer coefficients using neural networks *Int. J. Heat Mass Transfer* **39** 2329
- [43] Zhu F, Chen J, Han Y and Ren D 2022 A deep learning method for estimating thermal boundary condition

- parameters in transient inverse heat transfer problem *Int. J. Heat Mass Transfer* **194** 123089
- [44] García-Esteban J J, Bravo-Abad J and Cuevas J C 2021 Deep learning for the modeling and inverse design of radiative heat transfer *Phys. Rev. Appl.* **16** 064006
- [45] Xi W, Lee Y-J, Yu S, Chen Z, Shiomi J, Kim S-K and Hu R 2023 Ultrahigh-efficient material informatics inverse design of thermal metamaterials for visible-infrared-compatible camouflage *Nat. Commun.* **14** 4694
- [46] Azarifar M, Ocaksonmez K, Cengiz C, Aydoğan R and Arik M 2022 Machine learning to predict junction temperature based on optical characteristics in solid-state lighting devices: a test on wleds *Micromachines* **13** 1245
- [47] Hu R, Iwamoto S, Feng L, Ju S, Hu S, Ohnishi M, Nagai N, Hirakawa K and Shiomi J 2020 Machine-learning-optimized aperiodic superlattice minimizes coherent phonon heat conduction *Phys. Rev. X* **10** 021050
- [48] Koric S and Abueidda D W 2023 Data-driven and physics-informed deep learning operators for solution of heat conduction equation with parametric heat source *Int. J. Heat Mass Transfer* **203** 123809
- [49] Isola P, Zhu J-Y, Zhou T and Efros A A 2017 Image-to-image translation with conditional adversarial networks *Proc. IEEE Conf. on Computer Vision and Pattern Recognition* pp 1125–34
- [50] Tsang P W M and Poon T-C 2013 Novel method for converting digital fresnel hologram to phase-only hologram based on bidirectional error diffusion *Opt. Express* **21** 23680
- [51] Liu K, He Z and Cao L 2021 Pattern-adaptive error diffusion algorithm for improved phase-only hologram generation *Chin. Opt. Lett.* **19** 050501
- [52] Bakaric M, Miloro P, Javaherian A, Cox B T, Treeby B E and Brown M D 2021 Measurement of the ultrasound attenuation and dispersion in 3D-printed photopolymer materials from 1 to 3.5 MHz *J. Acoust. Soc. Am.* **150** 2798
- [53] Mikhail A S, Negussie A H, Graham C, Mathew M, Wood B J and Partanen A 2016 Evaluation of a tissue-mimicking thermochromic phantom for radiofrequency ablation *Med. Phys.* **43** 4304
- [54] Cline H E, Hynynen K, Hardy C J, Watkins R D, Schenck J F and Jolesz F A 1994 Mr temperature mapping of focused ultrasound surgery *Magn. Reson. Med.* **31** 628